

**UNCLASSIFIED**

**AD 409 278**

**DEFENSE DOCUMENTATION CENTER**

**FOR**

**SCIENTIFIC AND TECHNICAL INFORMATION**

**CAMERON STATION, ALEXANDRIA, VIRGINIA**



**UNCLASSIFIED**

NOTICE: When government or other drawings, specifications or other data are used for any purpose other than in connection with a definitely related government procurement operation, the U. S. Government thereby incurs no responsibility, nor any obligation whatsoever; and the fact that the Government may have formulated, furnished, or in any way supplied the said drawings, specifications, or other data is not to be regarded by implication or otherwise as in any manner licensing the holder or any other person or corporation, or conveying any rights or permission to manufacture, use or sell any patented invention that may in any way be related thereto.

Interim Report 4

Covering the Period 1 March to 31 May 1963

## TUNNEL CATHODES FOR MICROWAVE TUBES

Prepared for:

AERONAUTICAL SYSTEMS DIVISION  
AIR FORCE SYSTEMS COMMAND  
WRIGHT-PATTERSON AIR FORCE BASE, OHIO

CONTRACT AF 33(657)-8721

By: D. V. Geppert B. V. Dore

STANFORD RESEARCH INSTITUTE

MENLO PARK, CALIFORNIA

\*SRI

409 278

CATALOG

AS AD No.

409278

STANFORD RESEARCH INSTITUTE  
MENLO PARK, CALIFORNIA

SRI

June 1963

Interim Report 4 | Covering the Period 1 March to 31 May 1963

## TUNNEL CATHODES FOR MICROWAVE TUBES

Prepared for:

AERONAUTICAL SYSTEMS DIVISION  
AIR FORCE SYSTEMS COMMAND  
WRIGHT-PATTERSON AIR FORCE BASE, OHIO


CONTRACT AF 33(657)-8721

By: D. V. Geppert B. V. Dore

SRI Project No. 4125

Approved:

  
PHILIP RICE, MANAGER PHYSICAL ELECTRONICS LABORATORY

  
J. D. NOE, DIRECTOR ENGINEERING SCIENCES DIVISION

Copy No...10..

## ABSTRACT

---

The equipment modifications and improvements made during the past interval are described in detail. Two vacuum deposition systems are now in operation. One system is designed specifically for CdS work, and the other system for other insulating barrier materials. Both systems have quartz crystal film-thickness monitors in operational use. In both systems, the complete three-layer cathode structure can be fabricated completely in vacuum. In the case of the CdS system, the cathodes have to be tested in another vacuum system at the present time. In the other system, however, the cathodes fabricated *in vacuo* can then be tested without exposure to atmosphere.

The structures Au-SiO-Au, Mo-SiO-Mo, and Mo-CdS-Mo have been studied. The Mo-SiO-Mo structure is the most promising cathode so far tested. It shows potential for high efficiency and long life. Our future efforts will, therefore, be concentrated on this structure.

The calculations of the relaxation frequency of hot electrons and holes in metals and semiconductors have now been completed. In this report, the calculations for hot holes in metals are presented. In addition, numerical results have been calculated and presented in such a way that a comparison can be made with Quinn's theory.

## FOREWORD

---

This program was established by the Aeronautical Systems Division, Wright-Patterson Air Force Base, Ohio, at Stanford Research Institute under Contract AF 33(657)-8721 for the purpose of developing thin-film "tunnel" cathodes for use in microwave tubes.

At Stanford Research Institute the project supervisor is Philip Rice and the principal investigators are Donovan V. Geppert and Burnell V. Dore. Marian Hirsch, Robert Mueller, John Papacosta, and Robert Parker provided invaluable assistance in various experimental phases of the work. Drs. Marshall Sparks and Kazuko Motizuki, of Stanford University, collaborated in the theoretical work concerning hot carriers in solids.

This is ASD Project 4156, Task 415603; project monitor is Robert Harris (ASRNET-1) of the Electronic Technology Laboratory (ASRNET).

## CONTENTS

---

ABSTRACT . . . . .	ii
FOREWORD . . . . .	iii
LIST OF ILLUSTRATIONS . . . . .	v
I INTRODUCTION . . . . .	1
II TECHNICAL DISCUSSION . . . . .	2
A. Equipment . . . . .	2
1. Evaporation Systems . . . . .	2
2. Film-Thickness Measurement . . . . .	6
B. Cathode Structures and Results . . . . .	11
1. Au-SiO-Au Structures . . . . .	11
2. Mo-SiO-Mo Structures . . . . .	14
3. Mo-CdS-Mo Structures . . . . .	15
C. Range of Excited Electrons and Holes in Metals and Semiconductors . . . . .	17
1. Relaxation Frequency of Hot Holes in a Metal . . . . .	17
2. Numerical Results for Relaxation Frequency of Electrons and of Holes in a Metal . . . . .	24
III SUMMARY AND CONCLUSIONS . . . . .	27
IV PROGRAM FOR NEXT INTERVAL . . . . .	28
REFERENCES . . . . .	29
APPENDIX: EVALUATION OF THE INTEGRALS OVER $\theta$ AND $K$ . . . . .	30

## ILLUSTRATIONS

---

Fig. 1	Close-Up of Substrate in Position in Veeco System . . . . .	3
Fig. 2	Close-Up of Substrate, Showing Typical Structure . . . . .	3
Fig. 3	Cadmium Sulfide System with Mask Assembly . . . . .	5
Fig. 4	General View of Veeco Evaporation System . . . . .	7
Fig. 5	Block Diagram of Quartz Crystal Monitor . . . . .	7
Fig. 6	Schematic Diagram of Quartz Crystal Oscillator and Discriminator . . . . .	8
Fig. 7	Recording of a Typical Evaporation . . . . .	9
Fig. 8	Multiple-Beam Interferometer . . . . .	10
Fig. 9	Fringe Pattern in Multiple-Beam Interferometer . . . . .	11
Fig. 10	Variation of Emission Current with Time on Au-SiO-Au Cathode . . . . .	12
Fig. 11	Conduction Characteristics of Au-SiO-Au Cathode . . . . .	13
Fig. 12	Cathode and Anode Current Pulses on Au-SiO-Au Cathode . . . . .	13
Fig. 13	Conduction Characteristics of Mo-SiO-Mo Cathode . . . . .	16
Fig. 14	Cathode and Anode Current Pulses on Mo-SiO-Mo Cathode . . . . .	16
Fig. 15	Allowed Regions of Integration for Eq. (8) . . . . .	22
Fig. 16	The Relaxation Frequencies of the Hot Electrons and Hot Holes as a Function of $k/k_F$ and $r_s$ . . . . .	24
Fig. 17	Curves of the Imaginary Part of Electron Self Energy $E_I/E_F$ as a Function of Wave Vector $k/k_F$ for Comparison of Quinn's Result (Dotted) with Ours (Solid) . . . . .	26



## I INTRODUCTION

The objective of this program is the development of the thin-film capacitor cathode for application to microwave tubes. The capacitor cathode is comprised of a metal-insulator-metal sandwich, in which one of the metals is a thin film. The insulator film is sufficiently thin so that a few volts bias will generate hot electrons. A portion of these hot electrons can be emitted into vacuum from the thin metal film.

The salient features of this type of cathode are:

- (1) Essentially instantaneous starting (or stopping), and the ability to be pulsed or otherwise modulated;
- (2) Potentially long life, because the structure can be kept cold;
- (3) Potentially high current density and high emission efficiency; and
- (4) Potentially low noise.

The first of these anticipated features has been demonstrated on all cathodes constructed and tested.

Significant improvements in life and noise have been made during the past quarter. The emission efficiency under pulsed conditions is comparable to conventional oxide-coated thermionic emitters for low duty-cycle operation.

## II TECHNICAL DISCUSSION

### A. EQUIPMENT

#### 1. EVAPORATION SYSTEMS

Two separate evaporation stations are currently in operation. The Veeco system, with the electron beam power source, is used for general purposes; a smaller system is used for fabricating CdS structures, and evaporating other materials that would contaminate the larger system.

##### a. VEECO SYSTEM

The Veeco system was designed so that devices could be fabricated and subsequently tested without breaking the vacuum. A stage has been installed in the bell jar to support the substrate, the substrate temperature element, a rotating mask assembly, and a quartz crystal monitor (see Fig. 1). As indicated in Interim Report 3, the Veeco system includes a Temescal electron beam power source and a flange to provide for more controls and connections to the bell jar.

The mask assembly is a circular disk, rotated by a stainless steel cable, coupled to a rotary feed-through in the flange. It has six positions, located by means of a Teflon detent on the stage that engages holes in the mask assembly. Small Teflon buttons maintain a spacing of 0.015 inch between the rotating disk and the stage.

The three masks for fabricating the cathodes (illustrated in Interim Report 3) fit into openings in the disk. Two of the extra positions in the disk are fitted with blanks, which serve as shutters to control the evaporation, and to permit outgassing of evaporation sources. An insulated anode for diode emission tests is located in the remaining position on the disk. Voltage is applied to the anode through a probe, which contacts a projection on the underside of the anode when the anode is in position for a test.

The glass substrates are prepared in advance to facilitate testing after fabrication without breaking vacuum. Figure 2 illustrates the technique that has been adopted for this purpose. Using an abrasive drill,

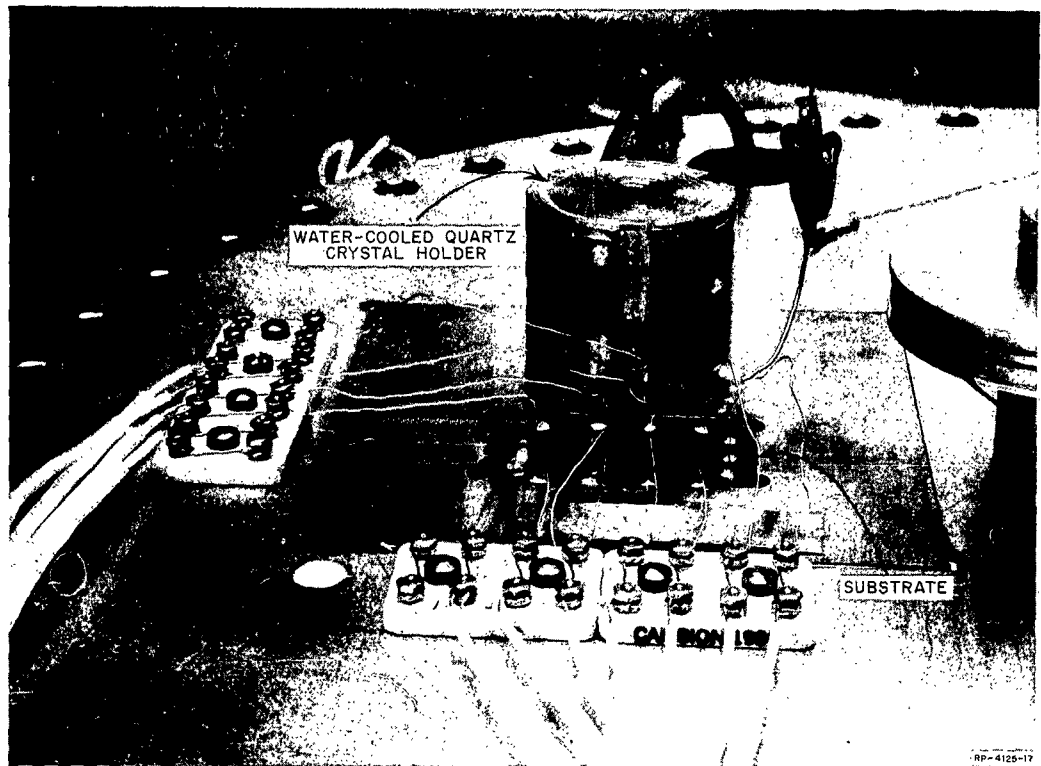


FIG. 1 CLOSE-UP OF SUBSTRATE IN POSITION IN VEECO SYSTEM

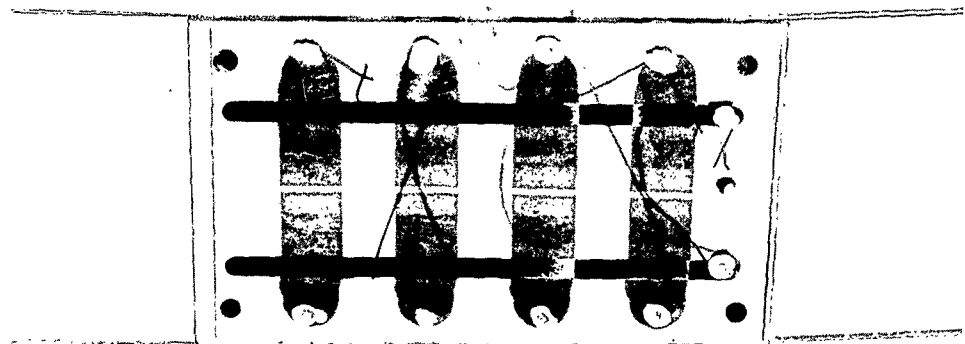


FIG. 2 CLOSE-UP OF SUBSTRATE, SHOWING TYPICAL STRUCTURE

small holes are drilled in the glass slide so that the evaporated metal strips will overlap these holes. Short nickel wire studs are imbedded in a conductive epoxy (Waldman No. 3021B) in these holes. Small, short wires connect these studs to terminal blocks on the stage, from which shielded leads make connections to octal headers (see Fig. 1).

The epoxy is cured under a heat lamp and has good vacuum properties at ordinary temperatures. Since it deteriorates at 150°C, this process is an experimental expedient that will be replaced by another technique when higher temperatures are involved. A process similar to that described by Feldman, *et al.*<sup>1\*</sup> is used in which a metal stud is formed in the hole in the substrate. Contact from the stud to the evaporated film is made by a previously-applied, fired gold film, derived from Hannovia Liquid Bright Gold.

The substrate temperature element is a water-cooled copper block with flexible couplings to the flange. A 180-watt cylindrical heating element (Hot Watt SC 752), incorporated into the block, is capable of raising the temperature of the substrate to 450°C.

In the Veeco system, the separation between the mask and the substrate is maintained at 0.040 inch. With operating vacuums in the  $10^{-6}$  torr range, and the method of mask location previously described, it has been found that the tolerance on pattern registration is approximately  $\pm 0.010$  inch, which is adequate for the present geometry.

#### b. CADMIUM SULFIDE SYSTEM

The cadmium sulfide system has been assembled primarily to fabricate cathodes with evaporated CdS barriers. It includes a moving mask arrangement and a quartz crystal monitor (see Fig. 3); at the present time, there is no provision for testing the cathodes in the same system.

Masks to produce the same configuration of cathode as the Veeco system were photoetched in a strip of beryllium copper. This strip moves on two rollers on the underside of a small stage that supports the substrate and the crystal monitor. The ends of the strip are attached by

---

\* References are listed at the end of the report.

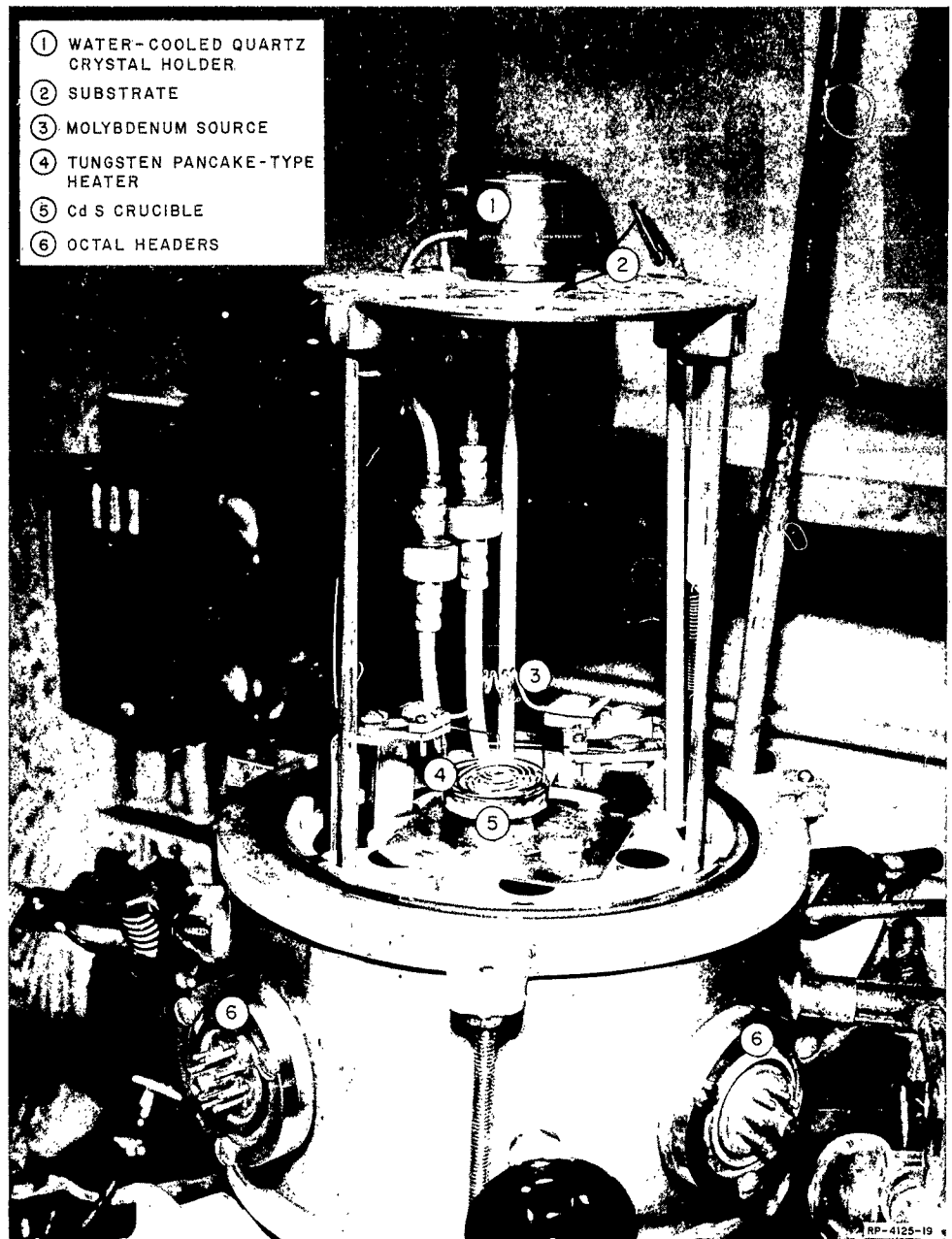


FIG. 3 CADMIUM SULFIDE SYSTEM WITH MASK ASSEMBLY

tension springs to a stainless steel cable, driven by a drum that is coupled to a rotary feed-through. A blank space in the strip provides a shutter during the evaporation cycle.

Various techniques for evaporating CdS were discussed in Interim Report 3. A large area source, comprising a pancake-type heating element above powdered CdS in a shallow alumina dish, was found to be most satisfactory for our purposes. With this arrangement, thick uniform films can be deposited at a rate of 100 Angstroms per minute, and according to the crystal monitor, the deposition rate is constant. No heat was applied to the substrate in addition to that radiated by the source, which was approximately 7 inches away.

## 2. FILM-THICKNESS MEASUREMENT

### a. QUARTZ CRYSTAL MONITOR

The monitor described in Interim Report 3 has been completed and is mounted in a mobile rack, shown on the right-hand side of Fig. 4. A block diagram of the system is shown in Fig. 5, and a full schematic is given in Fig. 6.

Each vacuum system has a quartz crystal in a water-cooled mount, which is connected to an octal header. The oscillator circuit is built into the external connection to the feed-through, and can be moved with the rest of the circuit from one evaporation station to the other.

The discriminator has been calibrated over a 90 kc interval and is very stable in operation. It has not been fully temperature-compensated, which will eventually be necessary to improve accuracy in monitoring lengthy evaporation cycles. The micrometer on the inductive tuner has 10,000 divisions, and the sensitivity of the over-all system is equivalent to one Angstrom of gold per division.

At the present time a Hewlett-Packard 425A Microvolt-Ammeter is used to monitor the output of the discriminator, and a Bausch & Lomb strip-chart recorder is coupled to the amplifier in the meter. In operation, the discriminator is detuned by an amount equivalent to the desired thickness of the film to be evaporated. When the output of the discriminator returns to zero, the evaporation is complete. A typical recording of an evaporation is shown in Fig. 7.

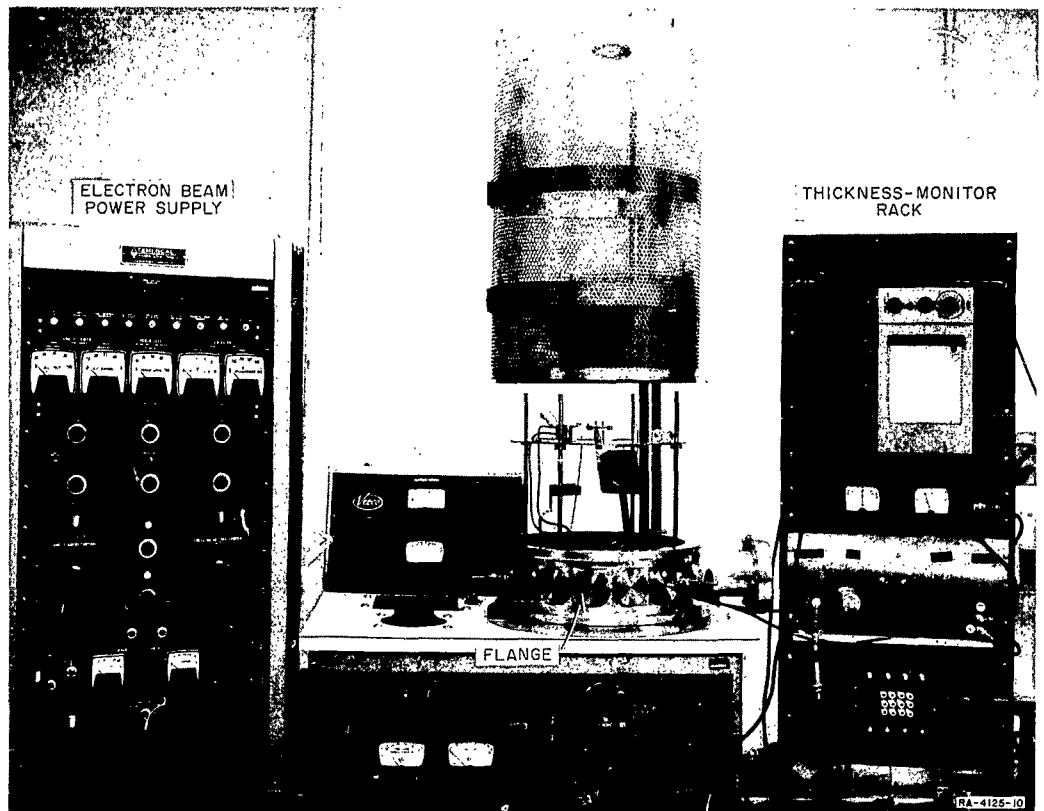


FIG. 4 GENERAL VIEW OF VEECO EVAPORATION SYSTEM

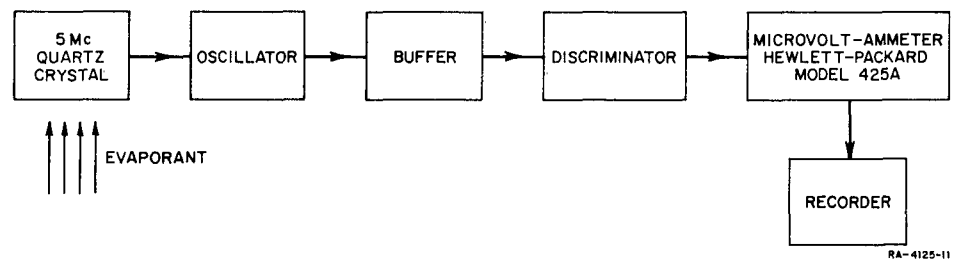
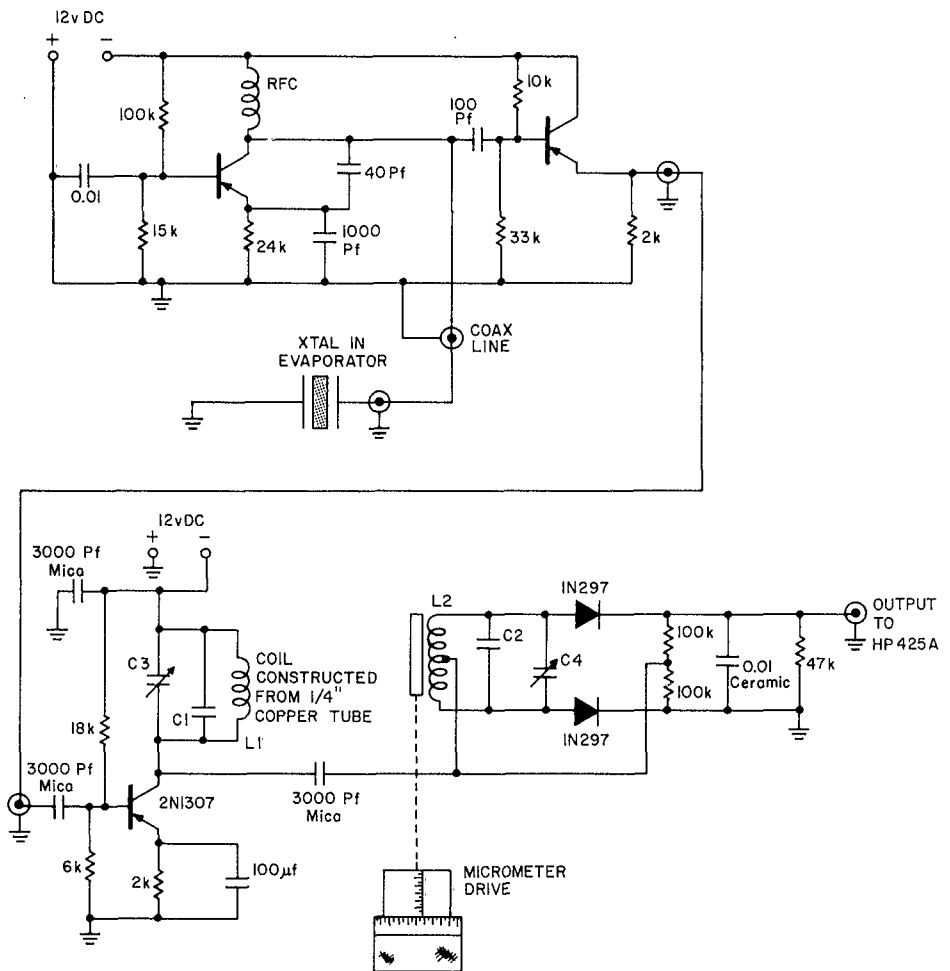


FIG. 5 BLOCK DIAGRAM OF QUARTZ CRYSTAL MONITOR



L1, C1, C3 TUNED TO 5mc  
L2, C2, C4 TUNED FOR FREQUENCY DESIRED

RA-4125-12

FIG. 6 SCHEMATIC DIAGRAM OF QUARTZ CRYSTAL OSCILLATOR AND DISCRIMINATOR



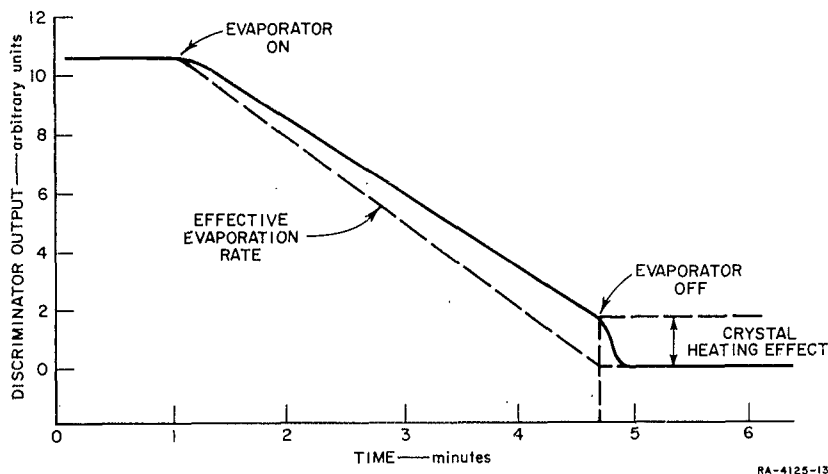


FIG. 7 RECORDING OF A TYPICAL EVAPORATION.

In this application, there is a heating effect when the crystal is exposed to the heat radiated during the evaporation of refractory and semi-refractory materials. The temperature coefficient of frequency of a high-quality AT-cut quartz crystal should be nearly zero from 0 to 20°C. Water-cooling the crystal holder does help, but, as shown in Fig. 7, it is necessary to anticipate this effect in order to evaporate a given amount of some materials.

#### b. MULTIPLE-BEAM INTERFEROMETER

The measurement obtained by the quartz crystal monitor depends upon  $\rho_E$ , the density of the evaporant. Since  $\rho_E$  is a function of film thickness and other deposition parameters, it is necessary to calibrate the crystal monitor by means of optical measurement of the films. A multiple-beam interferometer has been assembled for this purpose and is shown in Fig. 8.

A thallium spectral source is used, which has a principal line at 5350 Angstrom units. This light is collimated and split so that it is vertically incident on the stage of the microscope (on the left side of the photograph). Fizeau fringes are formed by an extremely thin wedge of air between the slide to be examined and a partially reflecting slide. The fringe pattern is displaced at the step formed by the edge of the

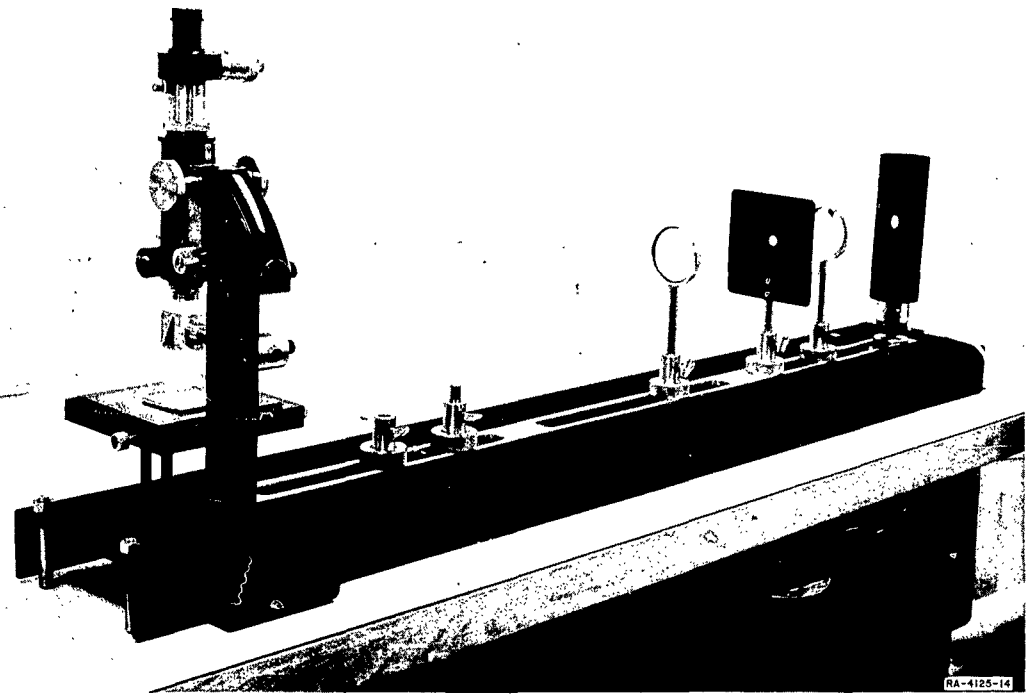


FIG. 8 MULTIPLE-BEAM INTERFEROMETER

film to be measured (see Fig. 9). The thickness of the film that produced the displacement shown would be given by the relationship

$$t = \frac{d}{s} \times \frac{\lambda}{2}$$

where  $\lambda$  is the wavelength of the monochromatic source.

The microscope has a 20-power micrometer eye piece and a 3-power objective. With this arrangement, the maximum deviation in measurement is  $\pm 17.5$  Angstrom units. This will be improved with the use of a simple jig to hold the slides, which will reduce the air gap and increase the separation between adjacent fringes.

Although the absolute measurement of very thin films is subject to some error, it should be noted that the equipment that has been

set up for monitoring film thickness does facilitate reproducibility. This is considered very important in fabricating thin-film cathode structures, particularly in the case of the barrier layer and the top electrode.

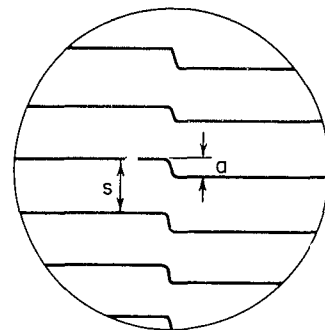
## B. CATHODE STRUCTURES AND RESULTS

### 1. Au-SiO-Au STRUCTURES

Several sets of Au-SiO-Au cathodes have been fabricated and tested. A set consists of 12 cathodes on one substrate, produced by the new masks described in Interim Report 3. First, three bottom gold stripes, about 500 Angstrom units thick, were deposited. Then, three SiO stripes on the order of 500 Angstrom units were evaporated over the gold stripes through a second mask. Finally, four top gold stripes, approximately 150 Angstrom units thick, were evaporated perpendicular to the bottom stripes. The top gold layer had a resistance of about ten ohms/square. The substrate was pre-wired for all the necessary connections to the cathodes. An anode was then placed in position and vacuum emission tests made.

In almost every case, it was found that the cathodes were shorted initially. The shorts could generally be removed by discharging a capacitor across the cathode, or by pulsing the cathodes from a low-impedance pulse generator. At this point, vacuum emission could be obtained from about 75% of the cathodes. However, the emission was erratic and very noisy. Invariably, the emission, as well as the cathode current, would decrease irreversibly with time and disappear completely within about an hour. Figure 10 shows the variation with time on a typical cathode.

Visible inspection of the dead cathodes under a binocular microscope revealed the presence of a multitude of pinholes through the films. Evidently, gold and SiO had evaporated from these small areas until all electrical contact to the cathodes had been lost along the edges of the active area where the top and bottom gold films overlapped.



RA-4125-15

FIG. 9 FRINGE PATTERN IN MULTIPLE-BEAM INTERFEROMETER

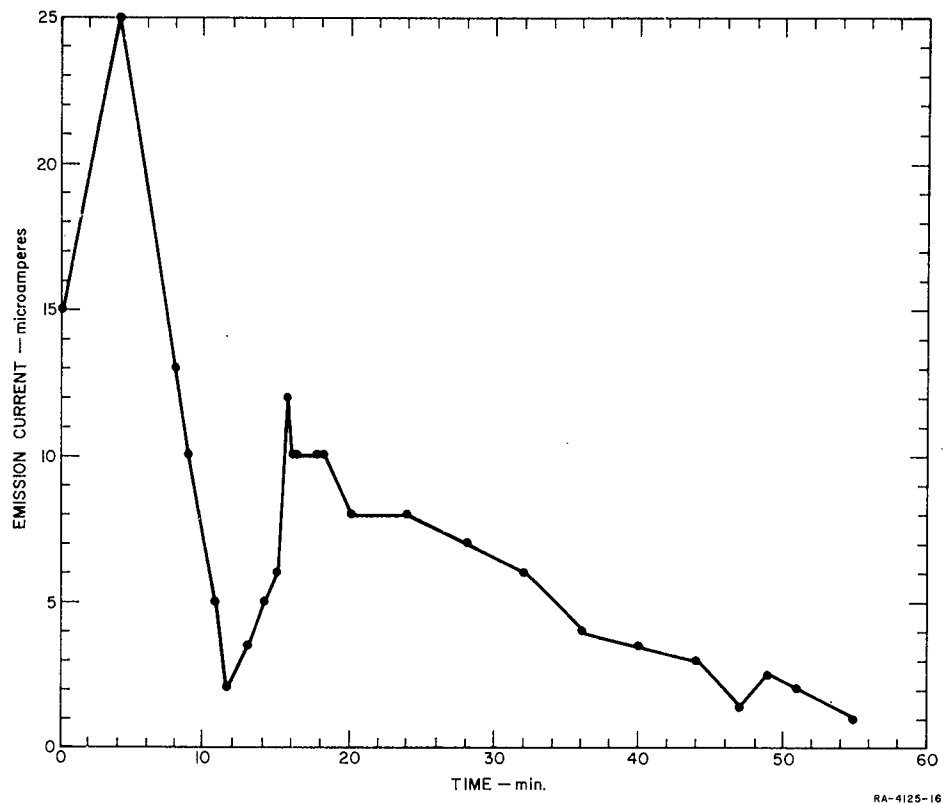
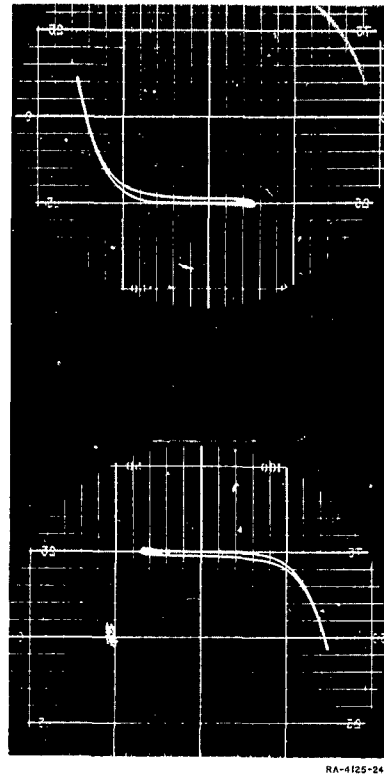


FIG. 10 VARIATION OF EMISSION CURRENT WITH TIME ON  $\text{AuSiO-Au}$  CATHODE

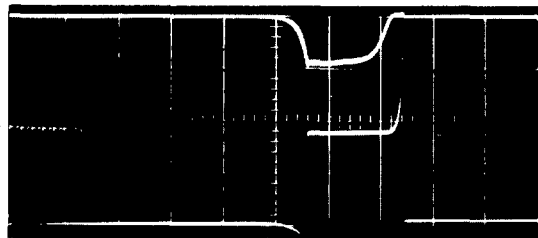
These results are very similar to those obtained earlier on  $\text{Au-CdS-Au}$  cathodes and strongly suggest that the gold is responsible for the behavior. A possible explanation is as follows: Localized heating at small areas causes the gold to diffuse into the  $\text{CdS}$  or the  $\text{SiO}$ . This makes the insulator thinner at these small areas, which increases the current and the localized heating. This is a regenerative effect which generates so much heat at localized areas that the gold and the insulating material are evaporated. The noisiness of the emitted electron stream could thus be associated with the fluctuations in the current at the small areas and even perhaps bursts of thermionic emission from the evaporating hot spots. Figure 11 shows typical current-voltage traces of the  $\text{Au-SiO-Au}$  cathode. Figure 12 shows cathode current and anode current waveforms.

The instability of the emission from the  $\text{Au-SiO-Au}$  cathodes prevented any meaningful data from being obtained concerning current-voltage characteristics of the vacuum diodes.



RA-4125-24

FIG. 11 CONDUCTION CHARACTERISTICS OF Au-SiO-Au CATHODE



RA-4125-25

FIG. 12 CATHODE AND ANODE CURRENT PULSES ON Au-SiO-Au CATHODE

The exact composition of the SiO films is not definitely known. It is believed that the films may contain excess oxygen. The composition may be  $\text{Si}_2\text{O}_3$  or  $\text{SiO}_2$  or combinations thereof. An attempt was made to determine the bandgap by making optical absorption measurements on the PE 112 spectrometer. The results indicate only that the bandgap is greater than about 3 electron volts, which is the high-energy limit of the present setup.

## 2. Mo-SiO-Mo STRUCTURES

The results obtained with the Au-SiO-Au cathodes suggested that the substitution of some other electrode material in place of the gold might provide improved life and lower noise. Our experience with molybdenum on another project has shown that Mo-Si interfaces are extremely stable, with no diffusion or chemical reactions occurring below about 800°C. Consequently, it was decided that the structure Mo-SiO-Mo should be investigated. A set of eight cathodes was fabricated, using the masks as described in Interim Report 3, but with the middle row of four cathodes deleted to avoid undesirable interactions found when all twelve cathodes were made.

A layer of about 500 Angstrom units of molybdenum was evaporated to form the two bottom stripes. A layer of about 200 Angstrom units of SiO was then evaporated over the molybdenum, followed by 150 Angstrom units of molybdenum to form the four molybdenum top layers.

In contrast to the Au-SiO-Au structures, none of the Mo-SiO-Mo structures were initially shorted. Vacuum emission yield was obtained on all these cathodes. They have been tested for several hours with no evidence of degradation or damage. The emission from these cathodes was much more stable and considerably less noisy than the emission from either Au-CdS-Au cathodes or Au-SiO-Au cathodes. These cathodes will be life-tested on a separate vacuum system using an ion pump.

Visible inspection of these Mo-SiO-Mo cathodes after several hours operation shows no evidence of pinholes. There may still be hot spots, as in the case of gold, but if there are, it appears that the molybdenum does not diffuse into the SiO as the gold did, thus preventing a runaway hot spot. In addition, the vapor pressure of molybdenum is much lower than that of gold, thus making the evaporation of molybdenum unlikely.

On the other hand, the major cause of hot-spots in the case of the Au-SiO-Au cathodes could be the diffusion of the gold at small localized areas. Thus, the use of molybdenum may prevent the initial formation of hot spots.

Figure 13 shows typical current-voltage characteristics, and Fig. 14 shows typical cathode and anode current pulses.

Additional Mo-SiO-Mo cathodes are being fabricated. Current-voltage data will be obtained on these. In addition, retarding-potential measurements will be made to determine the velocity distribution of the emitted electron stream. Selected cathodes will also be subjected to increasing current and voltage values to determine the characteristics at such values and the mode of failure which will occur.

### 3. Mo-CdS-Mo STRUCTURES

Because of the excellent results being obtained using molybdenum electrodes with SiO barriers, it was decided to use molybdenum instead of gold on the CdS structures as well as those using SiO.

The CdS cathodes are prepared in a separate evaporation system so as to avoid contamination of the Veeco system with cadmium or sulphur. In order to evaporate molybdenum in this system, it was expedient to resistance-heat a molybdenum wire coil to about 2200°C. On the first trial, the coil was positioned about 2 inches from the substrate in order to obtain a rapid deposition rate. A set of twelve cathodes was fabricated, using a sliding mask system having apertures identical to the masks used in the Veeco system.

It was found that the resistance of the molybdenum films was very high, on the order of 10,000 ohms/square. In addition, the films had a dark matte finish instead of a bright metallic luster. It was thought that this might be due to excessive heating of the substrate, causing agglomeration of the condensing molybdenum. Consequently, the molybdenum coil was moved away from the substrate to a distance of 6 inches for the next run. Another set of twelve cathodes was then fabricated, but the molybdenum films still had the matte appearance, coupled with a high resistance.

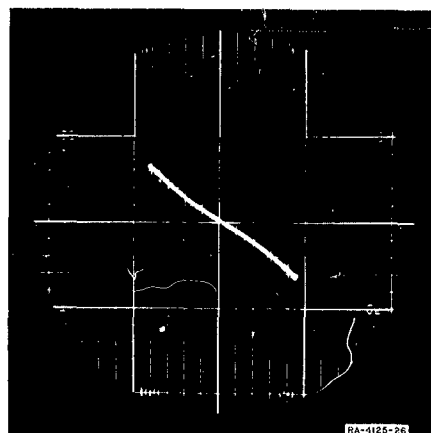


FIG. 13 CONDUCTION CHARACTERISTICS OF Mo-SiO-Mo CATHODE

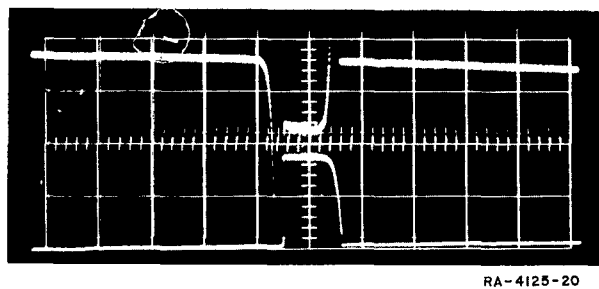


FIG. 14 CATHODE AND ANODE CURRENT PULSES ON Mo-SiO-Mo CATHODE



The pressure in the CdS system rises to about  $10^{-4}$  torr during the molybdenum evaporation. There is thus the possibility that the molybdenum films are heavily oxidized.

There is also the possibility of nitrides or sulfides of molybdenum being formed during the deposition.

In addition to this problem, it was found that the CdS is not evaporating properly through the mask. Without a mask, there is more heating of the substrate by intercepted radiation from the source. This substrate heating is doubtless beneficial in preventing excess cadmium in the CdS films. With a mask, however, the substrate heating is greatly reduced, and the films are not as clear yellow, showing evidence of excess cadmium. In addition, the apertures in the mask do not provide a clearcut delineation of the desired CdS areas. There is evidently considerable reflection of incident cadmium and  $S_2$  particles from the substrate and from the face of the mask, causing variations in thickness of the deposited films and deposits of CdS in unwanted areas.

In view of the difficulties being encountered with the CdS system, and in view of the excellent results being obtained on the Mo-SiO-Mo structures, it has been decided to shelve, temporarily, the CdS work and concentrate all the effort on the Mo-SiO-Mo system.

### C. RANGE OF EXCITED ELECTRONS AND HOLES IN METALS AND SEMICONDUCTORS

#### 1. RELAXATION FREQUENCY OF HOT HOLES IN A METAL

The following sections of the hot electron and hot hole study were included in Interim Reports 2 and 3:

Introduction

Interaction Hamiltonian

Relaxation Frequency of a Hot Electron in a Metal

Evaluation of Collision Integrals of a Hot Electron  
in a Metal

Limiting Case of Low Energy in a Metal

Limiting Case of High Energy and High Density in a Metal

Evaluation of Collision Integral in a Semiconductor

Limiting Case of Energy Near Threshold Value in a Semiconductor

In the present report, we consider the relaxation frequency of hot holes in a metal and give the results of numerical calculations for the relaxation frequency of hot holes and hot electrons in a metal.

In this section we calculate the relaxation frequency of a hot hole in a metal. We must consider the following process: The hole in the Fermi sea interacts with the electrons in the Fermi sea by the screened coulomb interaction given by

$$H' = \frac{4\pi e^2}{\Omega} \sum_{\mathbf{K}} \sum_{\mathbf{k} > \mathbf{k}'} \frac{1}{K^2 + k_c^2} c_{\mathbf{k}+\mathbf{K}}^\dagger c_{\mathbf{k}}^\dagger c_{\mathbf{k}'-\mathbf{K}} c_{\mathbf{k}'} \quad (1)$$

where  $c_{\mathbf{k}}^\dagger$  and  $c_{\mathbf{k}}$ , etc., represent a creation and an annihilation operator of an electron having wave vector  $\mathbf{k}$ . The operator  $c_{\mathbf{k}+\mathbf{K}}^\dagger c_{\mathbf{k}}^\dagger c_{\mathbf{k}'-\mathbf{K}} c_{\mathbf{k}'}$  in Eq. (1) corresponds to the transition process in which an electron in state  $\mathbf{k}$  moves to state  $\mathbf{k} + \mathbf{K}$  and another electron in the state  $\mathbf{k}'$  moves to the state  $\mathbf{k}' - \mathbf{K}$ . Then, an electron of wave vector  $\mathbf{k} + \mathbf{K}$  in the Fermi sea moves into the hole state of wave number  $\mathbf{k}$  and, at the same time, in order to conserve energy, an electron  $\mathbf{k}' - \mathbf{K}$  in the Fermi sea moves to the state  $\mathbf{k}'$  above the Fermi sea.

The transition probability corresponding to this process is given by

$$-\frac{2\pi}{\hbar} |\langle f_{\mathbf{k}} + 1, f_{\mathbf{k}'} + 1, f_{\mathbf{k}+\mathbf{K}} - 1, f_{\mathbf{k}'-\mathbf{K}} - 1 | H' | f_{\mathbf{k}}, f_{\mathbf{k}'}, f_{\mathbf{k}+\mathbf{K}}, f_{\mathbf{k}'-\mathbf{K}} \rangle|^2 \\ \times (1 - f_{\mathbf{k}'}) f_{\mathbf{k}+\mathbf{K}} f_{\mathbf{k}'-\mathbf{K}} \delta(\mathcal{E}_{\mathbf{k}} - \mathcal{E}_{\mathbf{k}'}) \quad (2)$$

where  $f$  is the Fermi distribution function; we assume the absolute zero Fermi distribution function

$$f = \begin{cases} 0 & \text{for energy greater than the Fermi energy} \\ 1 & \text{for energy less than the Fermi energy} \end{cases}$$

The relaxation frequency  $1/\tau_{\mathbf{k}}$  for hole  $\mathbf{k}$  is given by the integral of this transition probability over all allowed  $\mathbf{k}'$  and  $\mathbf{K}$  values.

The transition probability  $W(\mathbf{k}, \mathbf{K})$  of a hole  $\mathbf{k}$  associated with the momentum transfer  $\mathbf{K}$  is described by

$$W(\mathbf{k}, \mathbf{K}) = -\frac{4\pi}{\hbar} \left( \frac{4\pi e^2}{\Omega} \right)^2 \sum_{\mathbf{k}'} \frac{1}{(K^2 + k_c^2)^2} \delta(\epsilon_i - \epsilon_f) \quad (3)$$

The  $\delta$ -function in this equation is given by the expression

$$\delta(\epsilon_i - \epsilon_f) = \frac{m}{\hbar^2} \delta[\mathbf{k}' \cdot \mathbf{K} - (K^2 + \mathbf{k} \cdot \mathbf{K})] \quad ; \quad (4)$$

therefore, if we replace the sum over  $\mathbf{k}'$  by an integral,  $W(\mathbf{k}, \mathbf{K})$  becomes

$$W(\mathbf{k}, \mathbf{K}) = -CI(k, K, \cos \theta) \quad ,$$

where  $C$  is the numerical constant given by

$$C = 2 \frac{2\pi}{\hbar} \left( \frac{4\pi e^2}{\Omega} \right)^2 \frac{m}{\hbar^2} \left( \frac{\Omega}{8\pi^3} \right) = \frac{8me^4}{\hbar^3 \Omega} \quad (5)$$

and

$$I(k, K, \cos \theta) = 2\pi \frac{1}{(K^2 + k_c^2)^2 K} \int_{k_L}^{k_M} k' dk' \quad (6)$$

for

$$-1 \leq \frac{K + k \cos \theta}{k'} \leq 1 \quad (7)$$

In this integral  $I$ , the lower limit  $k_L$ , and the upper limit  $k_M$  are determined by the following conditions (a), (b), and (c).

Condition (a): By Eq. (7),

$$k' \geq k \cos \theta + K \quad \text{for} \quad \cos \theta \geq -\frac{K}{k}$$

$$k' \geq -(k \cos \theta + K) \quad \text{for} \quad \cos \theta \leq -\frac{K}{k} \quad ;$$

Condition (b):

$$k' \geq k_F ;$$

Condition (c): Since  $0 \leq |\mathbf{k}' - \mathbf{K}| \leq k_F$ , we have the following conditions:

$$(K^2 + 2\mathbf{k} \cdot \mathbf{K})^{1/2} \leq k' \leq (k_F^2 + K^2 + 2\mathbf{k} \cdot \mathbf{K})^{1/2}$$

and

$$\cos \theta \geq -\frac{k_F^2 + K^2}{2kK} , \quad \cos \theta \geq -\frac{K}{2k}$$

From Conditions (a), (b) and (c), the lower and upper limit of  $k'$  can be determined as a function of  $k$ ,  $K$  and  $\theta$  as follows:

$$\text{Case } A_1: \text{ If } \cos \theta \geq -\frac{K}{k} , \cos \theta \leq \frac{k_F - K}{k} , \cos \theta \geq -\frac{k_F^2 + K^2}{2kK}$$

and  $\cos \theta \geq -\frac{K}{2k}$ , then

$$k_L = k_F \quad \text{and} \quad k_M = (k_F^2 + K^2 + 2\mathbf{k} \cdot \mathbf{K})^{1/2}$$

$$\text{Case } A_2: \text{ If } \cos \theta \leq -\frac{K}{k} , \cos \theta \geq -\frac{k_F + K}{k} , \cos \theta \geq -\frac{k_F^2 + K^2}{2kK}$$

and  $\cos \theta \geq -\frac{K}{2k}$ , then

$$k_L = k_F \quad \text{and} \quad k_M = (k_F^2 + K^2 + 2\mathbf{k} \cdot \mathbf{K})^{1/2}$$

$$\text{Case } B_1: \text{ If } \cos \theta \geq -\frac{K}{k} , \cos \theta \geq \frac{k_F - K}{k} \quad \text{and} \quad \cos \theta \geq -\frac{k_F^2 + K^2}{2kK} ,$$

then

$$k_L = k \cos \theta + K \quad \text{and} \quad k_M = (k_F^2 + K^2 + 2\mathbf{k} \cdot \mathbf{K})^{1/2}$$

$$\text{Case } B_2: \quad \text{If } \cos \theta \leq -\frac{K}{k}, \quad \cos \theta \leq -\frac{k_F + K}{k}$$

$$\text{and } \cos \theta \geq -\frac{k_F^2 + K^2}{2kK}, \quad \text{then}$$

$$k_L = -(k \cos \theta + K), \quad \text{and} \quad k_M = (k_F^2 + K^2 + 2\mathbf{k} \cdot \mathbf{K})^{1/2}$$

Therefore, in the Cases  $A_1$ ,  $A_2$ ,  $B_1$  and  $B_2$  the integral  $I(k, K, \cos \theta)$  becomes as follows:

Case  $A_1$  and  $A_2$ :

$$I(k, K, \cos \theta) = -2\pi \frac{1}{K(K^2 + k_c^2)^{3/2}} \frac{1}{2} (K^2 + 2kK \cos \theta) \quad (8)$$

Case  $B_1$  and  $B_2$ :

$$K(k, K, \cos \theta) = -2\pi \frac{1}{K(K^2 + k_c^2)^{3/2}} \frac{1}{2} (k_F^2 - k^2 \cos^2 \theta) \quad (9)$$

Furthermore, in order to obtain the transition probability  $W(\mathbf{k}, \mathbf{K})$ , we must determine the allowable region of  $k$ ,  $K$  and  $\cos \theta$ . In addition to the Conditions (a), (b) and (c), the following condition is necessary:

Condition (d): The condition  $|\mathbf{k} + \mathbf{K}| \leq k_F$  implies that

$$\cos \theta \leq \frac{k_F^2 - k^2 - K^2}{2kK}$$

Then, for the Cases  $A_1$ ,  $A_2$ ,  $B_1$  and  $B_2$ , the following inequalities must be satisfied:

Case  $A_1$ :

$$\left( -\frac{K}{k}, -\frac{K}{2k}, -\frac{k_F^2 + K^2}{2kK} \right) \leq \cos \theta \leq \left( \frac{k_F - K}{k}, \frac{k_F^2 - k^2 - K^2}{2kK} \right)$$

Case  $A_2$ :

$$\left(-\frac{K}{2k}, -\frac{k_F + K}{k}, -\frac{k_F^2 + K^2}{2kK}\right) \leq \cos \theta \leq \left(-\frac{K}{k}, \frac{k_F^2 - k^2 - K^2}{2kK}\right)$$

Case  $B_1$ :

$$\left(-\frac{K}{k}, \frac{k_F - K}{k}, \frac{k_F^2 + K^2}{2kK}\right) \leq \cos \theta \leq \frac{k_F^2 - k^2 - K^2}{2kK}$$

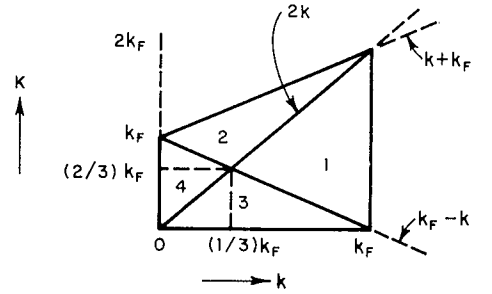
Case  $B_2$ :

$$-\frac{k_F^2 + K^2}{2kK} \leq \cos \theta \leq \left(-\frac{K}{k}, -\frac{k_F + K}{k}, \frac{k_F^2 - k^2 - K^2}{2kK}\right)$$

In the Cases  $A_2$ ,  $B_1$  and  $B_2$ , it is impossible to find a region of  $(k, K, \theta)$  that satisfies all of the inequalities.

For the Case  $A_1$ , the possible region of  $(k, K)$  can be divided into four regions, 1, 2, 3 and 4, and the allowed region of  $\cos \theta$  are different corresponding to each region as described in Fig. 15.

The relaxation frequency  $1/\tau$  of the hole now can be obtained by the integration of  $I(k, K, \theta)$  over all possible values of  $\theta$  and  $K$ . The integrals over  $\theta$  and  $K$  are evaluated in the Appendix. The results for the relaxation frequency  $1/\tau$  as a function of  $k$  are as follows:



Region 1:  $-\frac{K}{2k} \leq \cos \theta \leq -\frac{K^2 - (k_F^2 - k^2)}{2kK}$

Region 2:  $-1 \leq \cos \theta \leq -\frac{K^2 - (k_F^2 - k^2)}{2kK}$

Region 3:  $-\frac{K}{2k} \leq \cos \theta \leq 1$

Region 4:  $-1 \leq \cos \theta \leq 1$

RA-4125-21

FIG. 15 ALLOWED REGIONS OF INTEGRATION FOR EQ. (8)

For  $1/3 k_F \leq k \leq k_F$ :

$$1/\tau = -C(2\pi)^2 \frac{1}{2} \left( \frac{\Omega}{8\pi^3} \right) \times \{A_1[k_F - k, k + k_F] - D_1[2k, k + k_F] + D_2[2k, k + k_F] + D_1[0, k_F - k]\} \quad (10)$$

For  $0 \leq k \leq 1/3 k_F$ :

$$1/\tau = -C(2\pi)^2 \frac{1}{2} \left( \frac{\Omega}{8\pi^3} \right) \times \{A_1[k_F - k, k + k_F] - D_1[k_F - k, k + k_F] + D_2[2k, k + k_F] + D_1[0, 2k]\} \quad (11)$$

where the functions  $A_1$ ,  $D_1$ , and  $D_2$  are defined by

$$A_1[a, b] = \frac{(k^2 - k_F^2)^2}{8kk_c^3} \left\{ \left[ \tan^{-1} \frac{b}{k_c} - \tan^{-1} \frac{a}{k_c} \right] + \frac{k_c(b - a)(k_c^2 - ab)}{(k_c^2 + b^2)(k_c^2 + a^2)} \right\}$$

and Eqs. (A-8) and (A-9) of the Appendix. For a hole whose initial energy is very close to the Fermi energy, the relaxation frequency  $1/\tau$  can be approximated by only the  $A_1[k_F - k, k + k_F]$  term, the other terms being very small. Then for  $k \simeq k_F$ , we obtained the same expression as the relaxation frequency of a hot electron near the Fermi surface given by

$$1/\tau = -\frac{1}{4\pi} \frac{me^4}{\hbar^3} \frac{1}{(k_c/k_F)^3} \left\{ \tan^{-1} \frac{2}{(k_c/k_F)} + \frac{2(k_c/k_F)}{4 + (k_c/k_F)^2} \right\} \frac{(x^2 - 1)^2}{x} \quad (12)$$

where

$$x = \frac{k}{k_F}$$

For a hole that is created near the bottom of the conduction band,  $1/\tau$  can be approximated by only the  $D_2[2k, k + k_F]$  term, because other terms become zero as  $k \rightarrow 0$ . The results of numerical evaluation of the factors in Eq. (10) and Eq. (11) are given in the following section.

## 2. NUMERICAL RESULTS FOR RELAXATION FREQUENCY OF ELECTRONS AND OF HOLES IN A METAL

The results of the calculations for the relaxation frequencies of electrons and of holes in a metal are conveniently illustrated in the graphs of relaxation frequency as a function of the wave vector of the incident electron or hole in Fig. 16. The effect of electron density is given by the parameter  $r_s$  in the curves. These curves were obtained by numerically evaluating the expressions in Eq. (10) and Eq. (11) for the hole relaxation frequency and the corresponding electron expressions given in Interim Report 3.

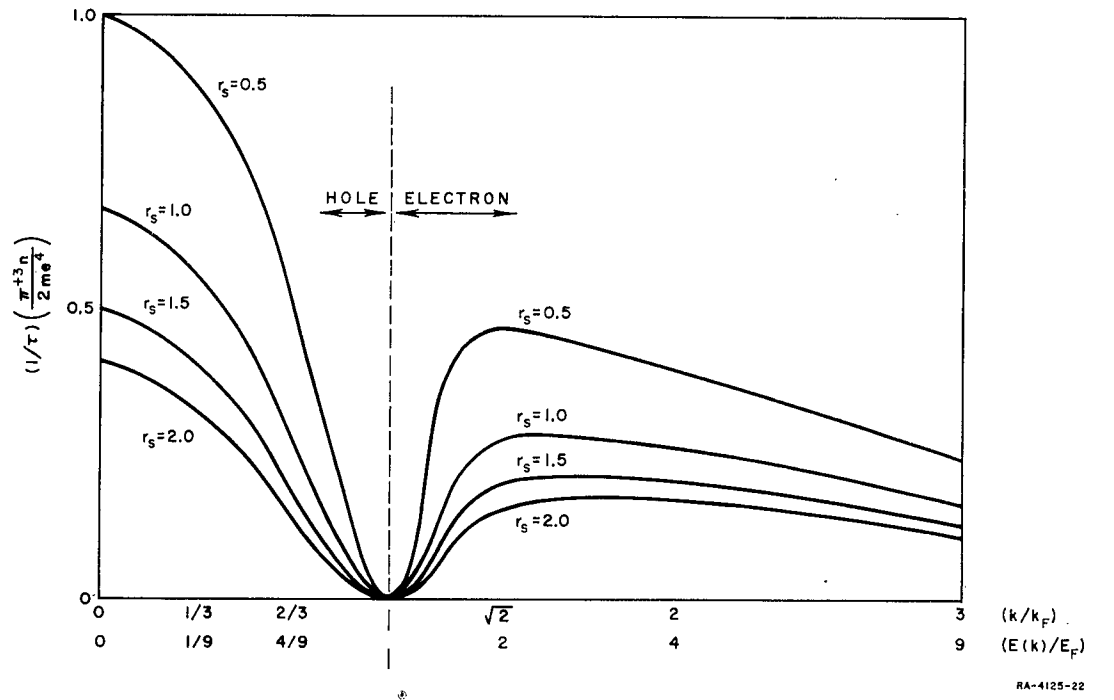


FIG. 16 THE RELAXATION FREQUENCIES OF THE HOT ELECTRONS AND HOT HOLES AS A FUNCTION OF  $k/k_F$  AND  $r_s$



Quinn<sup>2</sup> calculated  $E_I/E_F$  as a function of  $k/k_F$  for the case of  $r_s \approx 2$ ,  $E_F \approx 12$  electron volts, where  $E_I$  is the imaginary part of the self-energy of an incoming electron and is related to the relaxation frequency  $\tau$  by the relation  $2E_I/\hbar = 1/\tau$ . In order to compare our result with Quinn's, we show  $E_I/E_F [= (\hbar/2E_F)(1/\tau)]$  as a function of  $k$  in Fig. 17. In obtaining this figure we used the high density relation

$$\frac{k_c}{k_F} = (\gamma r_s)^{1/2},$$

where

$$\gamma = \frac{4\alpha}{\pi} = 0.656,$$

between  $k_c/k_F$  and  $r_s$ , which gives  $(k_c/k_F) = [(0.656)(2)]^{1/2} = 1.14$  for  $r_s = 2$ . We believe that  $(k_c/k_F) = 0.73$  obtained from the relation<sup>3</sup>

$$\left(\frac{k_c}{k_F}\right)^2 = \frac{\alpha r_s}{\pi} \left[ \left(2 + \frac{k_c}{k_F}\right) \ln \left(1 + 2 \frac{k_F}{k_c}\right) - 2 \right], \quad (13)$$

would be a better value; the value of  $k_c/k_F = 1.14$  was used in order to make a valid comparison of our result with Quinn's.

We summarize our conclusions:

- (1) In the high-density case, our result exactly agrees with the result of Quinn's self-consistent dielectric constant approximation for the low-energy limit. This means that the screened coulomb potential and the dielectric constant approximations both are valid only in the high-density and low-energy limit. The validity of the screened coulomb potential's approximation for the high-energy electron is not clear.
- (2) In the low-density case (for example  $r_s = 2$ ); our result and Quinn's result do not agree, even for low-energy electrons. Our calculation gives a shorter mean free path than Quinn's. The dielectric constant approximation is not valid in the low-density limit. The screened-coulomb potential approximation is valid in the high-density case, but in the low-density limit our approximation also becomes invalid for the following reasons. The Born approximation for the transition

probability has been used, and this is valid only when the potential energy is smaller than the kinetic energy. This appears to be the case only in the high-density limit. In a partial wave resistivity calculation, Abrahams<sup>4</sup> found that the transition probability method overestimates the scattering by a factor of five. Furthermore, even if we used the screening constant  $k_c$  as a phenomenological parameter, we related this  $k_c$  to  $r_s$  by Eq. (13). Strictly speaking, this relation (13) is useful only in the high-density limit.

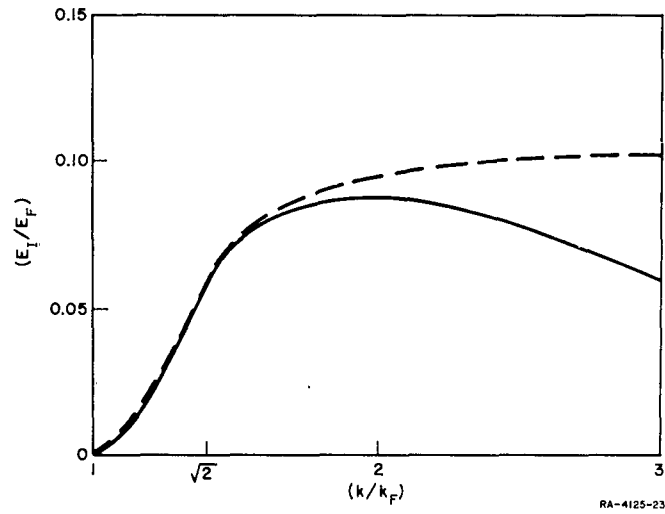


FIG. 17 CURVES OF THE IMAGINARY PART OF ELECTRON SELF ENERGY  $E_I/E_F$  AS A FUNCTION OF WAVE VECTOR  $k/k_F$  FOR COMPARISON OF QUINN'S RESULT (DOTTED) WITH OURS (SOLID)

### III SUMMARY AND CONCLUSIONS

The improved equipment and facilities for fabricating and testing thin film cold cathodes has been built and tested. This equipment permits fabrication and testing of cathode structures in vacuum without exposure to air. A special system for CdS permits fabrication but not testing in vacuum. Quartz crystal monitors in both systems permit monitoring of film thicknesses during deposition.

Au-SiO-Au cathodes were fabricated and tested. These cathodes yielded reasonable values of efficiency, but were unstable, noisy, and had short life. These problems have been attributed to the migration and diffusion of gold.

Mo-SiO-Mo cathodes were then fabricated and tested. These cathodes yielded efficiencies at least as high as the Au-SiO-Au cathodes, but the stability was higher and the noise lower. The initial tests indicate that these structures may be capable of long life.

Mo-CdS-Mo cathodes were also fabricated and tested, but a multitude of problems remain to be solved on these structures. Consequently, this work has been temporarily shelved in favor of the more promising Mo-SiO-Mo structures.

The theoretical calculations of the mean free path of hot electrons and holes has been completed. A comparison has been made with Quinn's result which indicates that the new theory is more accurate in the low density range.

#### IV PROGRAM FOR NEXT INTERVAL

From the results obtained so far on the Mo-SiO-Mo cathodes, it is clear that molybdenum is the best electrode metal so far tested. It has many desirable properties for the thin-film cathode:

- (1) High electrical conductivity;
- (2) Good mean free path for hot electrons (about as good, apparently, as gold);
- (3) Low vapor pressure;
- (4) High melting point; and
- (5) Low diffusion rates.

The only disadvantage of molybdenum compared to gold is the higher chemical activity. This may place a restriction on the choice of the insulating barrier material. Silicon monoxide and molybdenum appear to be compatible, and work during the next interval will therefore be concentrated on the structure Mo-SiO-Mo. The optimum thickness of the SiO film will be determined. Also, the optimum thickness of the molybdenum surface film will be determined. The mean free path of hot electrons in molybdenum will be measured by evaporating successively thicker molybdenum surface films.

The uniformity of the emission will be determined by accelerating the beam to a fluorescent screen to provide a magnified image of the emission. The designs for this work have been completed, and it should be under way soon.

Optimized cathode structures will be subjected to low work function surface treatments to enhance the emission current density and emission efficiency.

Arrangements have been made to incorporate special cathodes into low-level metal-ceramic traveling-wave tubes provided by Microwave Electronics Corporation of Palo Alto, California. These tubes require only about 300 microamperes for operation.

## REFERENCES

±

1. Feldman, Charles, H. E. Culver, and Lawrence Davies, "Techniques for Making Electrical Contacts to Thin Films," *Rev. Sci. Inst.* **33**, p. 124 (January 1962).
2. Quinn, J. J., "Range of Excited Electrons in Metals," *Phys. Rev.* **126**, p. 1453 (May 15, 1962).
3. Sawada, K., K. A. Brueckner, N. Fukuda, and R. Brout, "Correlation Energy of Electron Gas at High Density: Plasma Oscillations," *Phys. Rev.* **108**, p. 507 (November 1, 1957).
4. Abrahams, E., "Electron - Electron Scattering in Alkali Metals," *Phys. Rev.* **95**, p. 839 (1 August 1954).

# APPENDIX

## EVALUATION OF THE INTEGRALS OVER $\theta$ AND $K$

In this appendix we evaluate the integrals over  $\theta$  and  $K$  of  $I(k, K, \cos \theta)$  of (31). The integral over  $\theta$  is

$$-\frac{K^2 - (k_F^2 - k^2)}{2kK} \int_{-(K/2k)}^{(K^2 + 2kK \cos \theta) \sin \theta d\theta} = \frac{(k_F^2 - k^2)^2}{4kK} \equiv J_1(K) \quad (\text{A-1})$$

$$-\frac{K^2 - (k_F^2 - k^2)}{2kK} \int_{-1}^1 (K^2 + 2kK \cos \theta) \sin \theta d\theta = \frac{(k_F^2 - k^2)^2 - K^4}{4kK} + K(K - k) \\ \equiv J_1(K) - M_1(K) + M_2(K) \quad (\text{A-2})$$

$$\int_{-(K/2k)}^1 (K^2 + 2kK \cos \theta) \sin \theta d\theta = K(K + k) + \frac{K^3}{4k} \equiv M_1(K) \quad (\text{A-3})$$

$$\int_{-1}^1 (K^2 + 2kK \cos \theta) \sin \theta d\theta = 2K^2 \equiv M_2(K) \quad (\text{A-4})$$

The integral over  $K$  is

$$\int_a^b \frac{K^2}{K(K^2 + k_c^2)^2} J_1(K) dK = A_1[a, b] \quad (\text{A-5})$$

$$\int_a^b \frac{K^2}{K(K^2 + k_c^2)^2} M_1(K) dK = D_1[a, b] \quad (\text{A-6})$$

$$\int_a^b \frac{K^2}{K(K^2 + k_c^2)^2} M_2(K) dK = D_2[a, b] \quad (\text{A-7})$$

where  $A_1[a, b]$  is given by (A-15) and

$$\begin{aligned} D_1[a, b] = & \frac{1}{2} \log \left( \frac{k_c^2 + b^2}{k_c^2 + a^2} \right) + \frac{(b - a)}{4k} - \frac{1}{2} \frac{k_c^2(b^2 - a^2)}{(k_c^2 + b^2)(k_c^2 + a^2)} \\ & + \left( \tan^{-1} \frac{b}{k_c} - \tan^{-1} \frac{a}{k_c} \right) \left( \frac{k}{2k_c} - \frac{3}{8} \frac{k_c}{k} \right) \\ & + \frac{k_c(b - a)(k_c^2 - ab)}{(k_c^2 + b^2)(k_c^2 + a^2)} \cdot \left( \frac{k_c}{8k} - \frac{k}{2k_c} \right) \end{aligned} \quad (\text{A-8})$$

and

$$D_2[a, b] = \log \left( \frac{k_c^2 + b^2}{k_c^2 + a^2} \right) - \frac{k_c^2(b^2 - a^2)}{(k_c^2 + b^2)(k_c^2 + a^2)} \quad (\text{A-9})$$

STANFORD  
RESEARCH  
INSTITUTE

MENLO PARK  
CALIFORNIA

## Regional Offices and Laboratories

Southern California Laboratories  
820 Mission Street  
South Pasadena, California

Washington Office  
808 17th Street, N.W.  
Washington 6, D.C.

New York Office  
270 Park Avenue, Room 1770  
New York 17, New York

Detroit Office  
1025 East Maple Road  
Birmingham, Michigan

European Office  
Pelikanstrasse 37  
Zurich 1, Switzerland

Japan Office  
911 Iino Building  
22, 2-chome, Uchisaiwai-cho, Chiyoda-ku  
Tokyo, Japan

## Representatives

Honolulu, Hawaii  
1125 Ala Moana Blvd.  
Honolulu, Hawaii

London, England  
19, Upper Brook Street  
London, W. 1, England

Milan, Italy  
Via Macedonio Melloni, 49  
Milano, Italy

Toronto, Ontario, Canada  
Room 710, 67 Yonge St.  
Toronto, Ontario, Canada